Dark quantum droplets and solitary waves in beyond-mean-field Bose-Einstein condensate mixtures

Matthew Edmonds ⬡ *

ARC Centre of Excellence in Future Low-Energy Electronics Technologies, School of Mathematics and Physics,
University of Queensland, St Lucia, QLD 4072, Australia
and Department of Physics and Research and Education Center for Natural Sciences, Keio University, Hiyoshi 4-1-1,
Yokohama, Kanagawa 223-8521, Japan

Quantum liquidlike states of matter have been realized in an ongoing series of experiments with ultracold Bose gases. Using a combination of analytical and numerical methods we identify the specific criteria for the existence of dark solitons in beyond-mean-field binary condensates, revealing how these excitations exist for both repulsive and attractive interactions, the latter leading to dark quantum droplets with properties intermediate between a dark soliton and a quantum droplet. The phenomenology of these excitations is explored within the full parameter space of the model, revealing a spatial profile of the excitation that differs significantly from the Zakharov-Shabat soliton, leading to a negative effective mass that is enhanced in the presence of the quantum fluctuations. Finally the dynamics of pairs of the excitations are explored, showing nonintegrable dynamics and dark soliton bound states in the attractive regime.

I. INTRODUCTION

Liquid states of matter give rise to a plethora of fluidic phenomena caused by the interaction of atoms with each other, external forces, and other matter [1]. For classical fluids, intermolecular potentials give rise to macroscopic consequences such as surface tension and viscosity, as well as transient effects like the Rayleigh-Taylor instability and turbulence—phenomena that can be observed on terrestrial [2] and astronomical [3] scales. The intrinsic properties of fluids depend critically on their thermodynamic environment; quantum liquids can also share some of the properties of their classical counterparts while also exhibiting unique and unexpected phenomena with no classical analog [4].

The last few years have seen a series of groundbreaking experiments with degenerate atomic Bose-Einstein condensates which have demonstrated the capacity of these intrinsically weakly correlated systems to manifest liquidlike states of matter in the form of quantum droplets, made from highly magnetic [5–8] mixtures [9–13] and also purely Lee-Huang-Yang [14–16] quantum gases. These surprising discoveries have been attributed to purely quantum-mechanical effects in the form of the Lee-Huang-Yang (LHY) correction [17], which provides the stabilization required to avoid instability originating from collisional forces.

* m.edmonds@uq.edu.au

While there has been intense focus on understanding the ground states of many-body systems, their excitations also play a crucial role in understanding their fundamental behavior. Recently there has been renewed experimental interest in realizing nonlinear excitations with quantum gases such as dark solitons [18–21] and domain walls [22,23] which provide insight into reduced dimensionality topology in a highly controllable setting. Such states could provide an important resource for future applications in atomtronics [24] as well as providing fundamental insight into the physics of lower-dimensional quantum systems [25].

Quantum gases possessing internal degrees of freedom represent an important testing ground for many-body phenomena. These additional degrees of freedom can facilitate unique quantum states that sensitively depend on the nature of the atomic interactions [26]. The presence of attractive interactions in these systems can ordinarily lead to the collapse of the quantum state; however, it was shown theoretically that such a system can in principle be stabilized by beyond-mean-field effects [27]. This stimulated an intense interest in the phenomenology of beyond-mean-field physics in these systems—here fundamental questions such as the role of dimensionality [28–30], confinement [31,32], dynamical [33–35], collective [36], coherent [37], and gauge couplings [38], as well as nonequilibrium [39,40] effects and phase separation [41] have provided key insights into the unusual liquidlike properties of these ultradilute droplets [42,43]. Complementary to their existence in degenerate atomic systems, droplet states have also been investigated in other systems such as photonic [44], optomechanical [45], as well as in the helium liquids [46].

While previous works have addressed aspects of the fundamental nature of liquidlike ground states in quantum gases, recent work has focused on investigating the excitations in

these systems which possess nontrivial phase windings such as kinks [47], vortices [48], and dark solitons in dipolar systems [49].

The purpose of this work is to study the properties of the excitations in beyond-mean-field Bose-Einstein condensates in one dimension, including elucidating the fundamental criteria for the existence of dark quantum droplets (DQDs)— dark solitonlike excitations that exist in the beyond-mean-field model with attractive, rather than repulsive interactions in the cubic-quadratic Schrödinger system, as well as characterizing their fundamental properties with a complimentary combination of numerical and analytical approaches.

The paper is organized beginning with a description of the theoretical model describing the beyond-mean-field Bose-Einstein condensate mixture in Sec. II, including the basic solutions and conserved quantities that this model accommodates. The crossover from a dark soliton to the dark quantum droplet is explored in Sec. III, including a comparison of the droplets analytical and numerical properties in terms of the droplet's size, integrals of motion, and effective mass, as well as the dynamics of individual and pairs of dark solitary waves in this system. The paper concludes with a summary and outlook in Sec. IV.

II. BEYOND-MEAN-FIELD MODEL

The energy of $N = N_\uparrow + N_\downarrow$ Bose particles with mass m forming a two-component homogeneous atomic Bose-Einstein condensate can be written as

$$E_{3D} = \int d^3\mathbf{r} \left[\frac{\hbar^2}{2m} \sum_j |\nabla \Psi_j(\mathbf{r})|^2 + \sum_{j,k} \frac{g_{jk}}{2} n_j(\mathbf{r}) n_k(\mathbf{r}) \right], \tag{1}$$

where $j, k \in \{\uparrow, \downarrow\}$, $g_{jk} = 4\pi \hbar^2 a_{jk}/m$ defines the scattering parameter between atoms, and $n_j(\mathbf{r}) \equiv |\Psi_j(\mathbf{r})|^2$ defines the atomic density for component j. In order to understand the effect of beyond-mean-field effects, the underlying many-body Hamiltonian is diagonalized within the standard Bogoliubov–de Gennes formalism for the weakly interacting limit. After integrating out the transverse spatial degrees of freedom the one-dimensional ground state energy density is obtained as [28]

$$E_{1D} = \frac{(\sqrt{g_{\uparrow\uparrow}} n_\uparrow - \sqrt{g_{\downarrow\downarrow}} n_\downarrow)^2}{2} + g\delta g \frac{(\sqrt{g_{\downarrow\downarrow}} n_\uparrow + \sqrt{g_{\uparrow\uparrow}} n_\downarrow)^2}{(g_{\uparrow\uparrow} + g_{\downarrow\downarrow})^2}$$
$$- \frac{2\sqrt{m}}{3\pi\hbar} (g_{\uparrow\uparrow} n_\uparrow + g_{\downarrow\downarrow} n_\downarrow)^{3/2}, \tag{2}$$

where $g = (g_{\uparrow\uparrow} n_\uparrow + g_{\downarrow\downarrow} n_\downarrow)/n$, $\delta g = g_{\uparrow\downarrow} + \sqrt{g_{\uparrow\uparrow} g_{\downarrow\downarrow}}$, and $n = n_\uparrow + n_\downarrow$ [29]. Assuming an equal number of atoms in the spin mixture such that $n_\uparrow = n_\downarrow \equiv n$ and equal intercomponent interaction strengths $g_{\uparrow\uparrow} = g_{\downarrow\downarrow} \equiv g$, Eq. (2) simplifies to $E_{1D} = \delta g n^2 - 4\sqrt{2m}(gn)^{3/2}/(3\pi\hbar)$. Then within the local density approximation an effective equation of motion can be derived from the chemical potential $\mu_{QF}[\psi] = \partial E_{1D}/\partial N$ giving

$$i\hbar \frac{\partial \psi}{\partial t} = \left[\frac{\hat{p}_x^2}{2m} - u\hat{p}_x - \frac{\sqrt{2m}}{\pi\hbar} g^{3/2} |\psi| + \delta g |\psi|^2 \right] \psi, \tag{3}$$

where u defines the excitation's velocity in the moving frame. Equation (3) describes the dynamics of the binary system in

the equal (miscible) spin limit in the form of a cubic-quadratic nonlinear Schrödinger system. Let us consider the fundamental solutions of Eq. (3) in the limits of interest, $g \to 0$ with $\psi(\mu, x \to \pm\infty) = \pm\sqrt{n_0}$ and for $g \neq 0$ with $\psi(\mu, x \to \pm\infty) = 0$. In the first limit the system is integrable with the well-known family of dark soliton solutions $\psi_{DS}(\mu_{DS}, x) = \sqrt{n_0}[\beta \tanh(\beta x/\xi_{DS}) + i\sqrt{1 - \beta^2}]$, where the healing length is $\xi_{DS} = \hbar/\sqrt{mn_0 \delta g}$ with velocity u, $\beta = \sqrt{1 - u^2}$ where $0 < u < c$, c is the speed of sound, and $n_0 = \lim_{x \to \infty} |\psi(\mu, x)|^2$ defines the constant asymptotic density. Then we consider the second situation where Eq. (3) possesses instead a quantum droplet solution [28]

$$\psi_{QD}(\mu, x) = \frac{\sqrt{n_0}\mu/\mu_{QD}}{1 + \sqrt{1 - \mu/\mu_{QD}} \cosh(\sqrt{-2\mu m}x/\hbar)}, \tag{4}$$

where the flat-topped droplet state forms as $\mu \to \mu_{QD}$ where $\mu_{QD} = -4mg^3/9\pi^2\hbar^2\delta g$. We consider the general situation where both $g \neq \delta g \neq 0$. As such the model, Eq. (3), has a number of important symmetries. From a physical point of view we consider the regularized versions of the atom number, momentum, and energy given respectively by

$$N = \int dx [n_0 - |\psi(x)|^2], \tag{5a}$$

$$P = \frac{i\hbar}{2} \int dx \left[\psi \frac{\partial \psi^*}{\partial x} - \psi^* \frac{\partial \psi}{\partial x} \right] - \hbar n_0 \Delta\phi, \tag{5b}$$

$$E = \int dx \left[\frac{\hbar^2}{2m} \left| \frac{\partial \psi}{\partial x} \right|^2 + \frac{\delta g}{2}(n_0 - |\psi|^2)^2 \right.$$
$$\left. - \frac{2\sqrt{2m}}{3\pi\hbar} g^{3/2} \left\{ |\psi|^3 - \frac{3}{2}\sqrt{n_0}|\psi|^2 + \frac{1}{2}\sqrt{n_0^3} \right\} \right], \tag{5c}$$

where the phase difference $\Delta\phi = \arg(+\infty) - \arg(-\infty)$. As well as the three integrals of motion, Eqs. (5), the model, Eq. (3), accommodates distinct dilation invariances in the limits $\delta g = 0$ and $g = 0$. A dilation transformation is a scaling such that $x \to \sqrt{\alpha}x$ and $t \to \alpha t$ for $\alpha \in \mathbb{R}_{>0}$, and will in general leave a Schrödinger system with a single nonlinearity $|\psi|^n$ invariant if $\psi(x, t) \to \alpha^{1/n}\psi(\sqrt{\alpha}x, \alpha t)$. Then, we can see that when $\delta g = 0$ the dark soliton solution obeys $\psi_D \to \sqrt{\alpha}\psi_D(\sqrt{\alpha}x, \alpha t)$ while for $g = 0$ the quantum droplet undergoes the dilation $\psi_{QD} \to \alpha\psi_{QD}(\sqrt{\alpha}x, \alpha t)$. The competition between the two length scales associated with the interaction parameters g and δg facilitates unusual phenomenology in this nonlinear system. From Eq. (3) we can define a set of dimensionless units appropriate for numerical simulations. Since the interactions can be either repulsive ($\mu > 0$) or attractive ($\mu < 0$) we expect the excitation's size to be of order $\sim \hbar/\sqrt{mn_0\delta g}$ when the mean-field van der Waals term dominates over the LHY term, while in the attractive regime the excitation's size is of order $\sim \hbar/\sqrt{m|\mu_{QD}|}$. Then, the healing length $\xi_0 = \hbar/\sqrt{m|\mu_0|}$ with $\mu_0 = -\sqrt{2mn_0g^3}/\pi\hbar + \delta g n_0$ defines the intrinsic length of the system, and from this a timescale $\hbar/|\mu_0|$ follows. The resulting dimensionless interaction strength used in the numerical simulations is $\sqrt{9|\mu_{QD}|/2n_0\delta g}$.

To understand how a particular value of the dimensionless interaction strength changes the sign of the interactions, we consider the homogeneous limit of Eq. (3) where $\psi(x, t) = \sqrt{n_0}\exp(-i\mu_0 t/\hbar)$, then the point at which the interactions
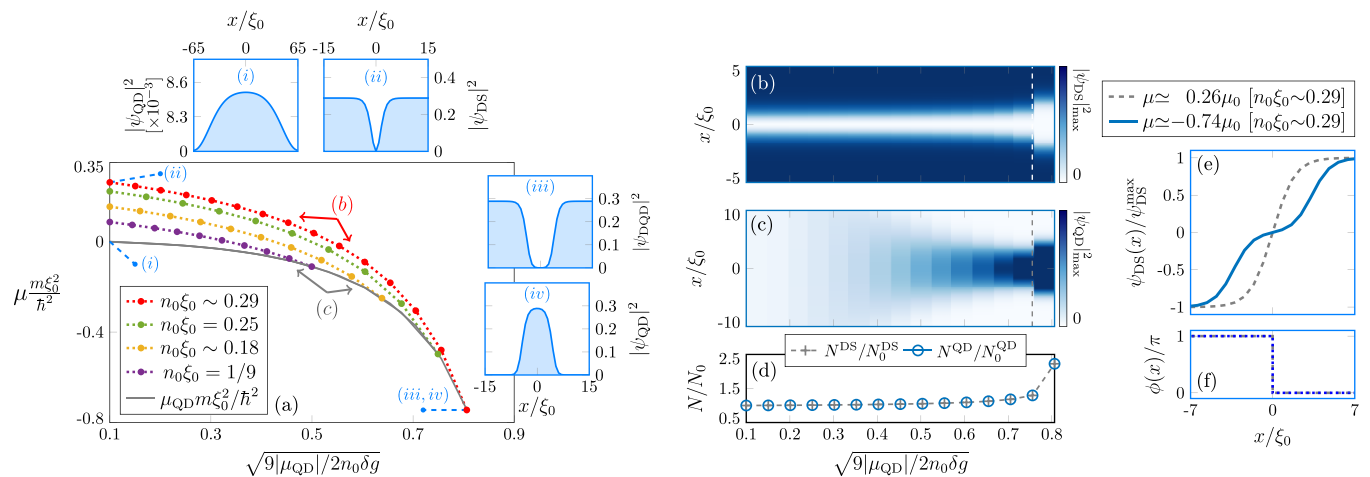
FIG. 1. Soliton to dark quantum droplet crossover. The transition from a dark soliton to the dark quantum droplet is shown in panel (a) for the fixed backgrounds $n_0\xi_0 = 0.29, 0.25, 0.18, 1/9$, with the insets (i)–(iv) showing selected solutions from (a). Heat maps of the excitation and ground state density with $n_0\xi_0 \sim 0.29$ are shown in (b) and (c), respectively. Panel (d) shows the atom number [Eq. (5a)] corresponding to (b) and (c). Comparisons of the excitation's wave function and phase are presented in panels (e) and (f).

change sign is μ_0, which corresponds to $\sqrt{9|\mu_{QD}|/2n_0\delta g} = \sqrt{\xi_0 n_0}$. Then for $0 < \sqrt{9|\mu_{QD}|/2n_0\delta g} < \sqrt{\xi_0 n_0}$ the interactions are repulsive ($\mu > 0$), while for $\sqrt{9|\mu_{QD}|/2n_0\delta g} > \sqrt{\xi_0 n_0}$ we have $\mu < 0$, attractive interactions. A comparison of the analytical values of the interaction strength at which μ changes sign shows close agreement with the numerical data presented in Fig. 1(a).

Using scattering lengths appropriate for ^{39}K [50] we can compute approximate values for the equilibrium density n_0 using [28]

$$n_0 = \frac{8}{9\pi^2}\frac{mg^3}{\hbar^2\delta g^2} \qquad (6)$$

with $m = m_{39\,K} = 6.5 \times 10^{-26}$ kg, $a_{\uparrow\uparrow} = a_{\downarrow\downarrow} \simeq 100a_0$, $|a_{\uparrow\downarrow}| \simeq 50a_0$ gives $\delta g \simeq 10^{-37}$ J m and $g = 7 \times 10^{-38}$ J m. Previous experiments with strongly confined quantum gases have been able to achieve optical confinement with strengths of order $\omega_r \simeq 2\pi \times 10$ kHz [51] which gives a one-dimensional density $n_0 \sim 1.6 \times 10^4$/m. Admittedly this is quite a small value, but optimistically could be improved in the future with the ever improving toolbox of quantum technologies for cold atom experiments [52]. Then, the dimensionless interaction parameter $\sqrt{9|\mu_{QD}|/2n_0\delta g} \sim 1$, similar to the values that will be used in this work.

III. DARK QUANTUM DROPLETS

A. Dark soliton to dark quantum droplet crossover

In this section we explore the nature of the solutions to Eq. (3) in the limit $u = 0$. Since we are interested in the excited states, we use an iterative (Newton-Raphson) approach to compute these states. An overview of the numerical procedure is given in the Appendix.

We explore the transition from a dark soliton excitation to the dark quantum droplet in Fig. 1. In panel (a) we solve the cubic-quadratic Schrödinger equation [Eq. (3)] as a function of the interaction strength for both the excited (dark soliton-like excitation) and the quantum droplet ground state. Each

dark soliton solution is computed using a Newton-Raphson method with fixed Neumann boundary conditions. From this, the atom number, Eq. (5a), is calculated. This in turn is used as the input for the ground state quantum droplet's atom number $N_{QD} = \int dx |\psi_{QD}(x)|^2$, so for a fixed value of the interaction strength in Fig. 1(a) $N_{DQD} = N_{QD}$. Each quantum droplet's ground state is computed using an imaginary time Fourier split-step method. The chemical potential is plotted for both situations, and for each fixed boundary condition, it is found that the chemical potential of the dark soliton eventually meets that of the droplet state. We can calculate the critical point at which this occurs by equating the quantum droplet's chemical potential μ_{QD} with the homogeneous chemical potential μ_0, which leads to the criterion

$$\sqrt{\frac{9|\mu_{QD}|}{2n_0\delta g}} = (1 - 10^{-\lambda})\frac{3}{2}\sqrt{n_0\xi_0} \qquad (7)$$

with corresponding critical chemical potential $\mu_{crit} = -n_0\delta g/2$. Very close to this point, the dark soliton acquires a profile resembling an inverted quantum droplet with a hollow central region, but with an asymmetric wave function. The final simulation point is chosen by including the prefactor $1 - 10^{-\lambda}$ in Eq. (7) with $\lambda = 3$ for Fig. 1 (for $\lambda \to \infty$ the size of the droplet diverges). Panels (i)–(iv) show a number of example density profiles taken from the red-dotted data ($n_0\xi_0 \sim 0.29$). Far from the transition point at weak attractive (repulsive) values of the chemical potential a broad quantum droplet (narrow dark soliton) is observed [panels (i) and (ii), respectively]. Then, very close to the point at which the chemical potentials cross, the dark soliton develops a wide hollow region around its core, while the droplet state at this point becomes narrow and tall [panels (iii) and (iv), respectively]. A heat map of the red-dotted transition data from (a) is shown in (b), along with the accompanying quantum droplet ground state data in panel (c), while the dashed lines in panels (b) and (c) correspond to the solutions (iii) and (iv) discussed above. Following this, panels (e) and (f) compare the solutions ψ_{DS}, scaled to the asymptotic spatial values and the accompany-

ing phase $\phi(x) = \tan^{-1}[\text{Im}(\psi_{\text{DS}})/\text{Re}(\psi_{\text{DS}})]$, respectively, for $\mu \simeq 0.32\mu_0$ (dark soliton) and $\mu \simeq -0.74\mu_0$ (dark quantum droplet). Panel (d) presents the atom number N_{DQD} [Eq. (5a)] for both situations, showing the gradual increase that occurs as the transition point is approached. Recent work has also studied the existence of dark solitonlike excitations in the binary LHY system (Refs. [47,48]). These works interpreted the excitation's unusual shape in terms of a pair of separating kink-antikink pairs.

B. Root-mean-squared width

The results presented in Fig. 1 reveal that as the chemical potential of the dark soliton approaches that of the quantum droplet, the soliton's profile resembled that of an inverted droplet. Previous experimental studies of the soliton to droplet crossover [11,53] have established that one can define a soliton at relatively small atom numbers, while for large atom numbers a quantum droplet emerges. We can perform a similar distinction here to understand the crossover from a dark soliton to a dark quantum droplet. From Fig. 1, (iii) and (iv), we can infer that

$$\lim_{\mu \to \mu_{\text{QD}}} (n_{\text{QD}}(\mu, x) + n_{\text{DQD}}(\mu, x)) = n_0. \tag{8}$$

Equation (8) will allow us to calculate observables of the dark quantum droplet state. The mean-squared width is an important characteristic which can be used to characterize the behavior of the dark droplet as the chemical potential approaches that of the quantum droplet's. Similarly to the regularized forms of the atom number, momentum, and energy [Eqs. (5a)–(5c)] we can also compute the mean-squared width from

$$\langle x^2 \rangle = \frac{1}{N_{\text{DQD}}(\mu)} \int_{-\infty}^{\infty} dx\, x^2 \left[n_0 - \lim_{\mu \to \mu_{\text{QD}}} n_{\text{DQD}}(\mu, x) \right]$$

$$= \frac{1}{N_{\text{DQD}}(\mu)} \int_{-\infty}^{\infty} dx\, x^2 \lim_{\mu \to \mu_{\text{QD}}} n_{\text{QD}}(\mu, x). \tag{9}$$

Here the second line of Eq. (9) has been written using Eq. (8). From here the known solution for the droplet $n_{\text{QD}}(\mu, x) \equiv |\psi_{\text{QD}}(\mu, x)|^2$ [Eq. (4)] can be used to obtain an expression for both the atom number $N_{\text{DQD}}(\mu)$ and the mean-squared width $\langle x^2 \rangle$ using the inversion formulas for the polylogarithms for the latter, yielding

$$\frac{\langle x^2 \rangle}{\xi_{\text{QD}}^2} = \frac{N_0}{N_{\text{DQD}}(\mu)} \frac{\mu_{\text{QD}}}{\mu} \left\{ \frac{1}{3} \left(\text{arsech}^3 \sqrt{1 - \frac{\mu}{\mu_{\text{QD}}}} + \pi^2 \right) \right.$$

$$\left. \times \text{arsech}\sqrt{1 - \frac{\mu}{\mu_{\text{QD}}}} \right) - \sqrt{\frac{\mu}{\mu_{\text{QD}}}} \left[\text{arsech}^2 \sqrt{1 - \frac{\mu}{\mu_{\text{QD}}}} + \frac{\pi^2}{3} \right] \right\}, \tag{10}$$

where $\xi_{\text{QD}} = \hbar/\sqrt{m|\mu_{\text{QD}}|}$ with the constant $N_0 = 2n_0\xi_{\text{QD}} = \sqrt{2n_0^2\hbar^2/m|\mu_{\text{QD}}|}$. Then the atom number $N_{\text{DQD}}(\mu)$ appearing in Eq. (10) can be evaluated in a similar manner, giving

$$\frac{N_{\text{DQD}}(\mu)}{N_0} = 2\,\text{artanh}\left[\frac{\sqrt{\mu/\mu_{\text{QD}}}}{1 + \sqrt{1 - \mu/\mu_{\text{QD}}}} \right] - \sqrt{\frac{\mu}{\mu_{\text{QD}}}}. \tag{11}$$

Using Eqs. (10) and (11) we can understand the intrinsic properties of the dark quantum droplet. First, let us derive the asymptotic behavior of Eqs. (10) and (11) when
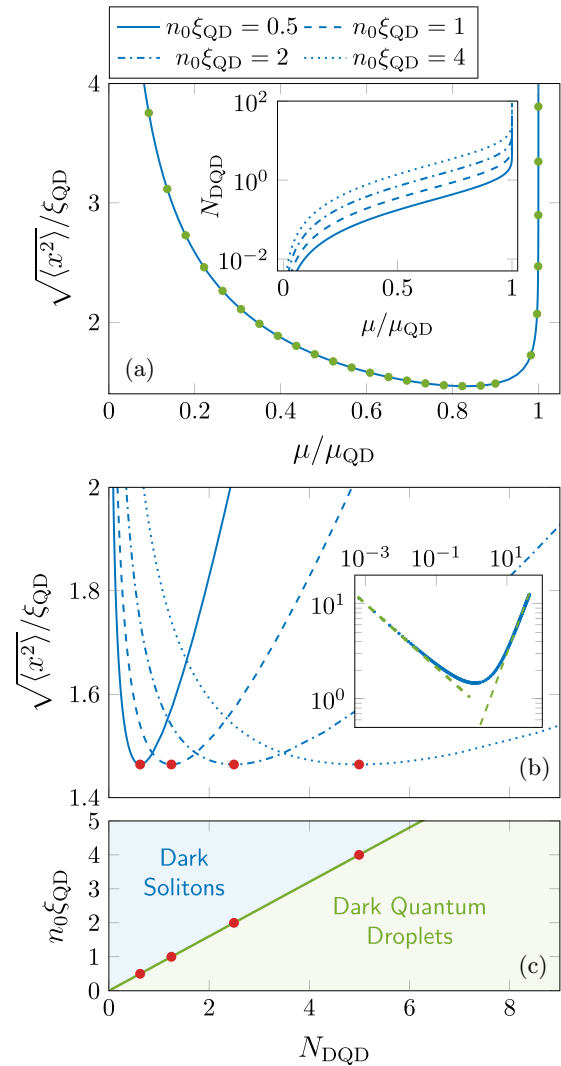

FIG. 2. Dark quantum droplet root-mean-squared width. Panel (a) shows Eq. (10), $\sqrt{\langle x^2 \rangle}/\xi_{\text{QD}}$, as a function of μ/μ_{QD}—the minima occurs for $\mu \simeq 0.8306\mu_{\text{QD}}$; while the inset shows Eq. (11) for several values of $n_0\xi_{\text{QD}}$. Panel (b) shows $\sqrt{\langle x^2 \rangle}/\xi_{\text{QD}}$ instead as a function of N_{DQD}, while the inset displays a log-log plot for $n_0\xi_{\text{QD}} = \frac{1}{2}$. The minima of $\sqrt{\langle x^2 \rangle}/\xi_{\text{QD}}$ in (b) are plotted in (c) (green solid) with the red circles corresponding to the locations of the four curves individual minima.

$N_{\text{DQD}} \gg 1$. For the atom number, one finds the relationship between the chemical potential and N_{DQD} is $N_{\text{DQD}}(\mu)/N_0 = \ln(2/\sqrt{1 - \mu/\mu_{\text{QD}}})$. Hence the atom number $N_{\text{DQD}}(\mu)$ diverges logarithmically as $\mu \to \mu_{\text{QD}}$. Expanding Eq. (10) for $\mu \to \mu_{\text{QD}}$ and using the asymptotic form of Eq. (11), the root-mean-squared width in the limit $N_{\text{DQD}} \gg 1$ is

$$\frac{\sqrt{\langle x^2 \rangle}}{\xi_{\text{QD}}} \underset{\mu \to \mu_{\text{QD}}}{=} \frac{N_{\text{DQD}}}{\sqrt{3}N_0}, \tag{12}$$

showing that the effective width of the dark quantum droplet diverges linearly in a fashion qualitatively similar to the quantum droplet [33]. Figure 2 shows the root-mean-squared width of the dark quantum droplet, Eq. (10). Panel (a) shows the behavior of the width $\sqrt{\langle x^2 \rangle}/\xi_{\text{QD}}$ as a function of the

chemical potential μ/μ_{QD}, while the inset shows the atom number, Eq. (11), for several values of the background density $n_0\xi_{\text{QD}} = \frac{1}{2}, 1, 2, 4$; increasing $n_0\xi_{\text{QD}}$ has the effect of giving an overall increase to N_{DQD}. Note that there is no dependency of $\langle x^2\rangle/\xi_{\text{QD}}^2$ on the background density $n_0\xi_{\text{QD}}$ when plotted as a function of the dimensionless chemical potential μ/μ_{QD}. The second panel (b) shows the root-mean-squared width $\sqrt{\langle x^2\rangle}/\xi_{\text{QD}}$ as a function of the atom number, for the same values of background density shown in the inset of (a). Increasing $n_0\xi_{\text{QD}}$ has the effect of stretching $\sqrt{\langle x^2\rangle}/\xi_{\text{QD}}$ such that the linear part $[N_{\text{DQD}}(\mu) \gg 1]$ associated with the dark quantum droplet occurs at larger values of $N_{\text{DQD}}(\mu)$. The minima of $\sqrt{\langle x^2\rangle}/\xi_{\text{QD}}$ also shift to larger values of $N_{\text{DQD}}(\mu)$ as $n_0\xi_{\text{QD}}$ is increased. The inset of Fig. 2(b) shows the dataset for $n_0\xi_{\text{QD}} = \frac{1}{2}$ in (b) in a log-log plot. The dashed lines show the asymptotic forms of Eq. (10) for $\mu/\mu_{\text{QD}} \to 0$, $\sqrt{\langle x^2\rangle} \sim N_{\text{DQD}}^{-1/3}$, $\mu/\mu_{\text{QD}} \to 1$, and $\sqrt{\langle x^2\rangle}/\xi_{\text{QD}} = N_{\text{DQD}}/(\sqrt{3}N_0)$ [54], the second of these limits being appropriate to the dark quantum droplet. The minima of $\sqrt{\langle x^2\rangle}/\xi_{\text{QD}}$ are plotted in (c) as a function of N_{DQD} (green solid) with the red circles corresponding to the locations of the four curves minima in (b). The shaded blue and green regions indicate the parameter regimes where we expect dark solitons and dark quantum droplets, respectively.

A comparison of the dark quantum droplet's analytical atom number and root-mean-squared width with the numerically obtained values is explored next in Fig. 3. Stationary state solutions to Eq. (3) are shown in (a) for $n_0\xi_0 = 0.36$. The interaction strength is chosen using Eq. (7) again using the prefactor $1 - 10^{-\lambda}$ with $\lambda = 1, 2, \ldots, 9$. The analytic atom number of Eq. (11) (solid blue) is plotted along with the equivalent values computed from the numerical (orange pluses) data in panel (b). Here good agreement is found as $\mu \to \mu_{\text{QD}}$. The root-mean-squared width $\sqrt{\langle x^2\rangle}/\xi_0$ is compared from Eq. (10) (solid green) and the numerical data (blue pluses). The agreement is found to improve as λ increases, and it was found that due to the underlying logarithmic divergence of $N_{\text{DQD}}(\mu)$ as $\mu \to \mu_{\text{QD}}$ obtaining a convergence between the analytical and numerical results in general requires very large λ, which becomes impractical for numerical simulations, but could be an interesting question to explore in a future experiment. The green solid and red dashed lines in (a) are computed from Eqs. (10) and (12), respectively. Panel (d) shows the dynamics of the $\lambda = 9$ solution, showing the stationary profile of the excitation. The green and red-dashed lines are plots of Eqs. (10) and (12), respectively. Note that these solutions show some similarity to recent work concerning vortices in two-component immiscible condensates [55–58].

C. Moving frame solutions and integrals of motion

In this section we investigate the solutions to the beyond-mean-field model in the moving frame such that $u \neq 0$ where u is the velocity in the moving frame and $\hat{H}_{\text{bMF}}$ denotes the beyond-mean-field Hamiltonian appearing in Eq. (3). In the limit that $g = 0$ we recover the well-known Zakharov-Shabat (ZS) solution [59], where the allowed solutions exist on the interval $0 \leqslant u < c_s$ where c_s is the speed of sound. The depth of the excitation is directly related to its velocity
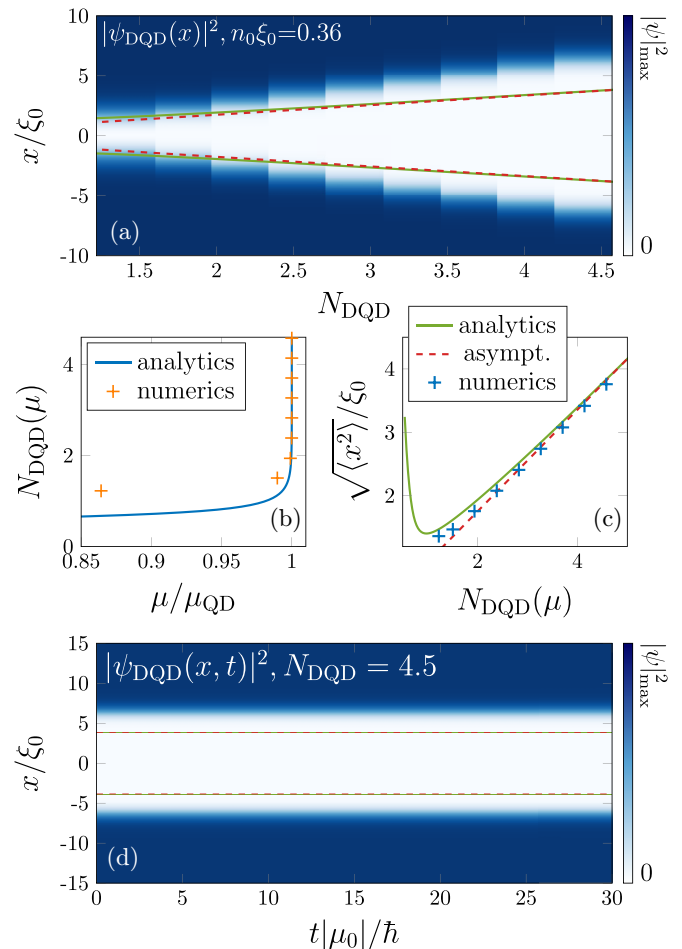

FIG. 3. Dark quantum droplet width comparison. Numerical solutions for the density $|\psi(x)|^2$ to Eq. (3) are shown in (a) for $n_0\xi_0 = 0.36$, with the green solid and red dashed lines computed from Eqs. (10) and (12). The atom number $N_{\text{DQD}}(\mu)$ as a function of the chemical potential μ/μ_{QD} is shown in (b) for the analytical result, Eq. (11) (solid blue), and numerical values (orange pluses), while (c) compares the root-mean-squared width $\sqrt{\langle x^2\rangle}/\xi_0$ computed using Eq. (10) (solid green), Eq. (12) (dashed red), and from the numerical values (blue pluses). Panel (d) shows the real-time propagation for $t_{\text{tot}} = 30\hbar/|\mu_0|$ of the final dataset from (a); here $N_{\text{DQD}} \sim 4.5$ ($\lambda = 9$).

through $\sqrt{n_{\text{min}}/n_0} = u/c_s$ where n_{min} is the density at the center of the phase twist and n_0 is the background, hence the faster the excitation moves the smaller its depth. Figure 4 presents the solutions to Eq. (3) as the dimensionless interaction strength is varied for a fixed background density $n_0\xi_{\text{QD}} = 0.25$ and velocity $u = 0.1\sqrt{|\mu_{\text{QD}}|/m}$. Panels (a) and (b) show the real $\text{Re}(\psi)$ and imaginary $\text{Im}(\psi)$ parts of the wave function. The top panel shows that the width of the real part increases with interaction strength, and the imaginary part shows a marked departure from the ZS solution, whose imaginary part, $\text{Im}(\psi) = \sqrt{n_0}u$, is a constant. We observe that the spatial structure of $\text{Im}(\psi)$ develops a minima localized at the center of the phase twist as the interaction strength increases. Panel (c) shows the chemical potential as a function of the interaction strength, with the three solutions (i)–(iii) highlighted. Then, the spatial structure of $\text{Im}(\psi)$ can
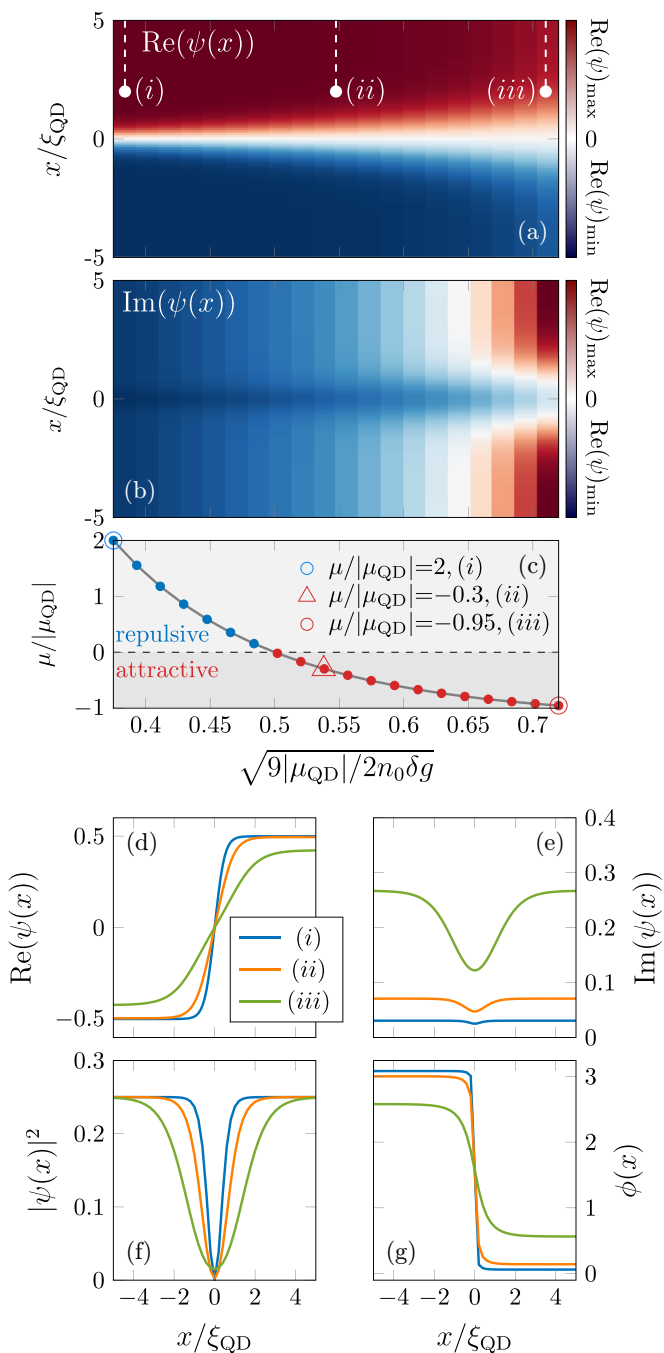
FIG. 4. Moving frame solutions. The real and imaginary parts of the solutions to Eq. (3) are presented as a function of $\sqrt{9|\mu_{\mathrm{QD}}|/2n_0\delta g}$, respectively, in panels (a) and (b). The chemical potential is shown as a function of the interaction strength in (c), with the individual highlighted points (i)–(iii). Individual solutions are shown in (d) [Re(ψ)] and (e) [Im(ψ)] for $\sqrt{9|\mu_{\mathrm{QD}}|/2n_0\delta g} = \{0.375, 0.538, 0.72\}$, while (f) and (g) show the same data in terms of density $|\psi(x)|^2$ and phase $\phi(x)$ corresponding to (i), (ii), and (iii) respectively.

be seen clearly in panel (e) where Im(ψ) evolves from an almost constant solution [blue data (i), $\sqrt{9|\mu_{\mathrm{QD}}|/2n_0\delta g} = 0.375$] to one with a pronounced minimum [green data (iii), $\sqrt{9|\mu_{\mathrm{QD}}|/2n_0\delta g} = 0.72$]. This behavior is attributed to the

presence of the quantum fluctuations. The density $|\psi|^2$ and phase data $\phi(x)$ corresponding to (d) and (e) are shown in (f) and (g).

Next we consider the effect varying the excitation's velocity u. To understand the role that quantum fluctuations play we can compute the three integrals of motion given by Eqs. (5a)–(5c). In the limit that $g \to 0$ these quantities can be computed exactly in analytical form, and are given by

$$N_{\delta g} = 2\xi_{\delta g}n_0\beta, \tag{13a}$$

$$P_{\delta g} = -\frac{2\hbar n_0 u\beta}{c_{\delta g}} + 2\hbar n_0 \arctan\left(\frac{c_{\delta g}\beta}{u}\right), \tag{13b}$$

$$E_{\delta g} = \frac{4}{3}n_0\hbar c_{\delta g}\beta^3. \tag{13c}$$

Here one has $\xi_{\delta g} = \hbar/\sqrt{mn_0\delta g}$ and $c_{\delta g} = \sqrt{n_0\delta g/m}$. Then one additional quantity can be obtained using the momentum $P_{\delta g}$, the excitations effective mass

$$m^* = \frac{\partial P}{\partial u} \tag{14}$$

which is given by $m^* = -4\hbar n_0\beta/c_{\delta g}$.

These four quantities are computed from Eqs. (5a)–(5c), and presented in panels (a)–(d) of Fig. 5 for several fixed interaction strengths ranging from repulsive $(\sqrt{9|\mu_{\mathrm{QD}}|/2n_0\delta g}, \mu/|\mu_{\mathrm{QD}}|) = (0.25, 54)$ to attractive $(\sqrt{9|\mu_{\mathrm{QD}}|/2n_0\delta g}, \mu/|\mu_{\mathrm{QD}}|) = (1.1, -0.37)$. The atom number N presented in (a) shows how the size of the excitation's core increases as the interaction strength is increased for a given velocity, eventually approaching zero as the speed of sound is reached. The momentum P is presented in (b). This quantity has a maximum value for $u = 0$ of $P/\hbar n_0 = \pi$, decreasing to zero as the speed of sound is reached. Increasing the interaction strength has the effect of "bending" this quantity downwards (see inset). Next, the regularized energy E is computed in (c). For a given velocity u, the interaction strength determines the curve with the largest energy, where the gap between the blue ($\mu/|\mu_{\mathrm{QD}}| = 54$) and green ($\mu/|\mu_{\mathrm{QD}}| = 3.2$) is caused by the large reduction in repulsive energy. The effective mass m^*, Eq. (14), is presented in panel (d), where the four datasets cross for $u/c_s \sim 0.32$. Then at velocities approaching $u = 0$ the effect of the quantum fluctuations increasingly causes this quantity to have a larger negative value (red data), which could be probed in a future experiment by measuring the oscillation frequency of a beyond-mean-field dark soliton in a harmonic trap [60]. For $0.32 \lesssim u/c_s < 1$ the quantum fluctuations instead enhance m^* for increasing interaction strength.

The final two panels of Fig. 5 show example space-time dynamics for data taken from the red points in panels (a)–(d), where $u/c_s = 0.75$ and 0.75 for (e) and (f), respectively. The scale of both heat maps is the same to highlight the different depths of the excitations. The insets show the initial density $|\psi(x, 0)|^2$ and phase $\phi(x)$ for (e) (blue data) and (f) (red data).

D. Excitation collision dynamics

The dark solitary wavelike excitation's static properties as presented in the previous sections are useful as a measure of their fundamental properties; however, a more comprehensive
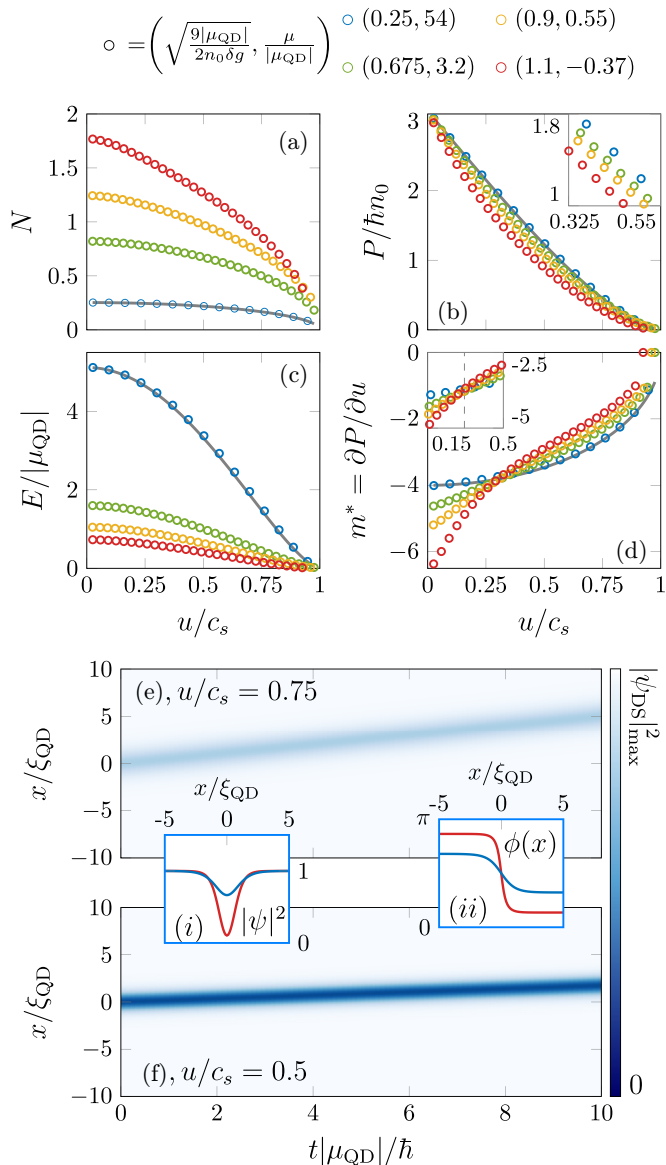
FIG. 5. Integrals of motion and dynamics. The four panels (a)–(d) show the calculated values of the quantities N, P, E, and m^* given by Eqs. (5a)–(5c) and (14); the key (top) indicates the values of the interaction strength $\sqrt{9|\mu_{QD}|/2n_0\delta g}$ and chemical potential $\mu/|\mu_{QD}|$ that each dataset corresponds to. Panels (e) and (f) show example dynamics taken from the red data for $u/c_s = 0.75, 0.25$, respectively. Insets (i) and (ii) display the initial density $|\psi(x,0)|^2$ and phase $\phi(x)$ from (e) and (f).

understanding of their behavior naturally incorporates their collision dynamics. We simulate the dynamics of pairs of moving frame dark solitary wavelike solutions to the beyond-mean-field model of Eq. (3). In particular, we consider a symmetric initial state of the form

$$\psi(x, t_0) = \psi_+(x - x_0, -v, \mu) + \psi_-(x + x_0, +v, \mu), \quad (15)$$

where x_0 defines the initial center of mass of the solution with velocity v and chemical potential μ. Figure 6 presents simulations of the collisions with a fixed background density of $n_0\xi_{QD} = 0.5$ for repulsive and attractive interaction

strengths. Panels (a)–(c) show collisions with weak repulsive interactions $\sqrt{9|\mu_{QD}|/2n_0\delta g} = 0.63$ with $\mu/\mu_{QD} = 0.55$ and $x_0/\xi_{QD} = 5$. Panel (a) shows a slow collision between two excitations, where $u/c_s^+ = 0.02$ ($c_s^\pm$ represents the speed of sound for repulsive $c_s^+ \simeq 1.74\sqrt{|\mu_{QD}|/m}$ and attractive $c_s^- \simeq 0.66\sqrt{|\mu_{QD}|/m}$ interactions) and there is an effective repulsion at the collision point [61,62]. For $u/c_s^+ = 0.5$ the excitations instead pass through each other, with a small amount of sound emission attributed to the proximity of these parameters to the attractive region of the parameter space, i.e., the effect of quantum fluctuations. Then panel (c) shows a faster collision with $u/c_s^+ = 0.75$.

Next we simulate collisions with attractive interactions, panels (d)–(f). Here $\sqrt{9|\mu_{QD}|/2n_0\delta g} = 1.1$ and $\mu/\mu_{QD} = -1.03$, and $x_0/\xi_{QD} = 10, 7.5, 5$ for (d)–(f), respectively. The excitation's dynamics are found to be qualitatively different to the case of repulsive interactions. In (d) and (e) we observe the formation of short-lived bound states of pairs of excitations. The existence of bound pairs of excitations is attributed to the balance of attractive and repulsive forces in Eq. (3). Below a critical velocity, the net attractive nonlinear interactions can accommodate a moleculelike state [63]. The length of the bound state t_{bs} depends on the excitation's initial velocity: for $u/c_s^- = 0.61$ we find $t_{tb} \simeq 50\hbar/|\mu_{QD}|$, and for $u/c_s^- = 0.64$ we find $t_{tb} \simeq 30\hbar/|\mu_{QD}|$ instead. The emission of radiation in the form of sound is observed in both cases, contributing to the eventual breaking of the bound states. Finally panel (f) shows a faster collision with $u/c_s^- = 0.76$ showing a quasielastic collision, with a reduced amount of sound emission. Animations of the solitary waves dynamics corresponding to the data in Figs. 6(c) and 6(e) are included as Supplemental Material [64].

IV. SUMMARY

In this work we have explored the phenomenology of dark quantum droplets and solitary waves, revealing the criteria for the existence of dark quantum droplets in beyond-mean-field Bose-Einstein condensate mixtures. The crossover from the dark soliton at weak repulsive to dark quantum droplets at attractive interaction strengths was found to depend sensitively on the interaction strength, a situation that was explored by comparing the analytical and numerical values of the excitation's root-mean-squared width, finding improving agreement as the transition point is approached. We then explored the beyond-mean-field solutions at finite velocity, revealing the departure of the excitation's shape from the Zakharov-Shabat solution. The integrals of motion of the excitation were computed, allowing the calculation of the excitation's effective mass, which was found to be strongly affected by the quantum fluctuations. Finally, the dynamics of pairs of the dark solitary waves were explored, revealing the existence of bound states in the attractive regime.

Due to the unusual profile of the dark quantum droplet, they could find useful application, for example, hosting qubits similar to proposals for dark solitons [65], as well as for matter-wave box traps [66], providing an alternate route to realizing matter-wave traps in a controllable environment.

For future studies and given the results presented in this work concerning the excitation's effective mass, it would
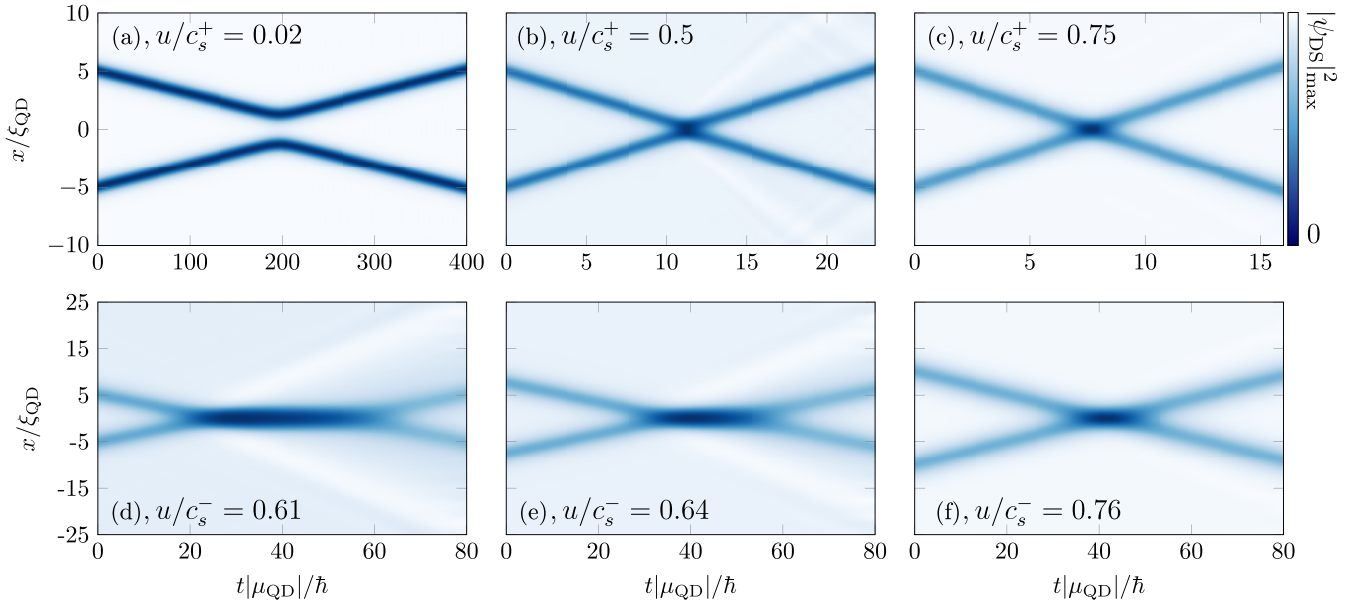
FIG. 6. Excitation collision dynamics. Initial collisional states are prepared according to Eq. (15) for fixed background $n_0\xi_{\text{QD}} = 0.5$. Panels (a)–(c) show collisions for repulsive interactions with $(\sqrt{9|\mu_{\text{QD}}|/2n_0\delta g}, \mu/\mu_{\text{QD}}) = (0.63, 0.55)$, and speed of sound $c_s^+ \simeq 1.74\sqrt{|\mu_{\text{QD}}|/m}$. Panels (d)–(f) show collisions for attractive interactions with $(\sqrt{9|\mu_{\text{QD}}|/2n_0\delta g}, \mu/\mu_{\text{QD}}) = (1.1, -1.03)$, and speed of sound $c_s^+ \simeq 0.66\sqrt{|\mu_{\text{QD}}|/m}$.

be intriguing to understand the behavior of dark quantum droplets in a harmonic trap, and how their oscillation frequency depends on the properties of the excitation [67]. The dynamical behavior, such as constructing Toda-like lattices, provides another future direction [68].

ACKNOWLEDGMENTS

APPENDIX: NEWTON-RAPHSON METHOD

Here we give an overview of the numerical method used to procure the dark quantum droplet solutions to the cubic-quadratic Schrödinger equation [Eq. (3) of the main text]. This type of approach has been used previously to study

excitations in superfluid systems such as vortices [69], and solitons in dipolar [70,71] and magnetic systems [72]. Our system differs from previous studies due to the presence of mixed nonlinearities. We consider a general scheme at finite velocity. First we write a function whose solutions we seek in the the Galilean-boosted frame as

$$F[\psi] = (\hat{H}_{\text{cqGPE}} - u\hat{p}_x - \mu)\psi, \tag{A1}$$

where u is the excitation velocity. Then Eq. (A1) can be translated into the iterative scheme

$$F_u(\psi^{p+1}) \approx F(\psi^p) + \sum_{v=1}^{N} \mathcal{J}_{u,v}\delta\psi_v \approx 0, \tag{A2}$$

where $\delta\psi = \psi^{p+1} - \psi^p$ and $\mathcal{J}_{u,v}$ defines the matrix elements of the Jacobian. The solutions to Eq. (A1) are in general complex valued, and since Newton-Raphson methods only work with real data we write the discrete $\psi(x)$ comprising N complex numbers as $2N$ real numbers such that $\text{Re}[\psi(x)] \equiv \psi_{j,0}$ and $\text{Im}[\psi(x)] \equiv \psi_{j,1}$, with the second subscript referring to the real and imaginary components. Then one can write the discrete form of Eq. (A1) as

$$f_{j,s} = -\frac{\hbar^2}{2m}\left[\frac{\psi_{j-1,s} - 2\psi_{j,s} + \psi_{j+1,s}}{\Delta x^2}\right] + (2s-1)\hbar u\left[\frac{\psi_{j+1,1-s} - \psi_{j-1,1-s}}{2\Delta x}\right]$$
$$+ \left\{-\frac{\sqrt{2m}}{\pi\hbar}g^{3/2}\sqrt{\psi_{j,0}^2 + \psi_{j,1}^2} + \delta g(\psi_{j,0}^2 + \psi_{j,1}^2)\right\}\psi_{j,s} - \mu\psi_{j,s}. \tag{A3}$$

The boundary conditions for the problem are treated as the Neumann type, such that

$$\left.\frac{d\psi}{dx}\right|_{x=\pm L} = 0, \tag{A4}$$

which translates into taking $\psi_{1,s} - \psi_{0,s} = 0$ and $\psi_{N+1,s} - \psi_{N,s} = 0$ for the kinetic term and $\psi_{2,s} - \psi_{0,s} = 0$ and $\psi_{N+1} - \psi_{N-1,s} = 0$ for the momentum operator. The matrix elements of the Jacobian appearing in Eq. (A2) are found from $\mathcal{J}_{k,r}^{j,s} = \partial f_{j,s}/\partial \psi_{k,r}$. Using $\partial \psi_{j,s}/\partial \psi_{k,r} = \delta_{j,k}\delta_{s,r}$ we obtain

$$
\mathcal{J}_{k,r}^{j,s} = -\frac{\hbar^2}{2m}\delta_{s,r}\left[\frac{\delta_{k,j-1} - 2\delta_{k,j} + \delta_{k,j+1}}{\Delta x^2}\right] + (2s-1)\delta_{1-s,r}\hbar u\left[\frac{\delta_{k,j+1} - \delta_{k,j-1}}{2\Delta x}\right] - \frac{\sqrt{2m}}{\pi\hbar}g^{3/2}\delta_{k,j}\left[\psi_{j,s}\frac{\delta_{0,r}\psi_{j,0} + \delta_{1,r}\psi_{j,1}}{\sqrt{\psi_{j,0}^2 + \psi_{j,1}^2}}\right.
$$

$$
\left. + \delta_{r,s}\sqrt{\psi_{j,0}^2 + \psi_{j,1}^2}\right] + \delta g\delta_{k,j}\left[2\psi_{j,s}(\delta_{0,r}\psi_{j,0} + \delta_{1,r}\psi_{j,1}) + \delta_{r,s}(\psi_{j,0}^2 + \psi_{j,1}^2)\right] - \mu\delta_{k,j}\delta_{s,r}, \tag{A5}
$$

which defines a $2N \times 2N$ matrix. Then stationary solutions can be obtained to Eq. (3) using Eqs. (A1)–(A5) using a tolerance-based approach for $\delta\psi$. As such we employ the Frobenius norm $||\delta\psi|| = \sqrt{\left(\sum_{j=1}^{2N} |\delta\psi_j|^2\right)}$ as a measure which is deemed convergence after falling below a predefined value, typically $||\delta\psi|| < 10^{-10}$. Computation of $\delta\psi$ at each step is accomplished by solving the linear system $\mathcal{J}\delta\psi =$

$-\mathbf{F}$ using a stabilized biconjugate gradient method which exploits the symmetry of the Jacobian to expedite the solution of the linear system by avoiding matrix inversion. The Newton-Raphson method requires an initial guess for $\psi(x)$, which we take as the dark soliton solution to the cubic Schrödinger equation. An example Python script for generating a dark quantum droplet can be found in [73].

[1] P. M. Chaikin and T. C. Lubensky, *Principles of Condensed Matter Physics* (Cambridge University Press, Cambridge, 1995).

[2] Y. A. Cengel, *Fluid Mechanics: Fundamentals and Applications* (McGraw-Hill, New York, 2017).

[3] C. Clarke and B. Carswell, *Principles of Astrophysical Fluid Dynamics* (Cambridge University Press, Cambridge, 2007).

[4] A. J. Leggett, Superfluidity, Rev. Mod. Phys. **71**, S318 (1999).

[5] H. Kadau, M. Schmitt, M. Wenzel, C. Wink, T. Maier, I. Ferrier-Barbut, and T. Pfau, Observing the Rosensweig instability of a quantum ferrofluid, Nature (London) **530**, 194 (2016).

[6] I. Ferrier-Barbut, H. Kadau, M. Schmitt, M. Wenzel, and T. Pfau, Observation of Quantum Droplets in a Strongly Dipolar Bose Gas, Phys. Rev. Lett. **116**, 215301 (2016).

[7] M. Schmitt, M. Wenzel, F. Böttcher, I. Ferrier-Barbut, and T. Pfau, Self-bound droplets of a dilute magnetic quantum liquid, Nature (London) **539**, 259 (2016).

[8] L. Chomaz, S. Baier, D. Petter, M. J. Mark, F. Wächtler, L. Santos, and F. Ferlaino, Quantum-Fluctuation-Driven Crossover from a Dilute Bose-Einstein Condensate to a Macrodroplet in a Dipolar Quantum Fluid, Phys. Rev. X **6**, 041039 (2016).

[9] C. R. Cabrera, L. Tanzi, J. Sanz, B. Naylor, P. Thomas, P. Cheiney, and L. Tarruell, Quantum liquid droplets in a mixture of Bose-Einstein condensates, Science **359**, 301 (2018).

[10] G. Semeghini, G. Ferioli, L. Masi, C. Mazzinghi, L. Wolswijk, F. Minardi, M. Modugno, G. Modugno, M. Inguscio, and M. Fattori, Self-Bound Quantum Droplets of Atomic Mixtures in Free Space, Phys. Rev. Lett. **120**, 235301 (2018).

[11] P. Cheiney, C. R. Cabrera, J. Sanz, B. Naylor, L. Tanzi, and L. Tarruell, Bright Soliton to Quantum Droplet Transition in a Mixture of Bose-Einstein Condensates, Phys. Rev. Lett. **120**, 135301 (2018).

[12] G. Ferioli, G. Semeghini, L. Masi, G. Giusti, G. Modugno, M. Inguscio, A. Gallemí, A. Recati, and M. Fattori, Collisions of Self-Bound Quantum Droplets, Phys. Rev. Lett. **122**, 090401 (2019).

[13] C. D'Errico, A. Burchianti, M. Prevedelli, L. Salasnich, F. Ancilotto, M. Modugno, F. Minardi, and C. Fort, Observation of quantum droplets in a heteronuclear bosonic mixture, Phys. Rev. Res. **1**, 033155 (2019).

[14] N. B. Jørgensen, G. M. Bruun, and J. J. Arlt, Dilute Fluid Governed by Quantum Fluctuations, Phys. Rev. Lett. **121**, 173403 (2018).

[15] F. Minardi, F. Ancilotto, A. Burchianti, C. D'Errico, C. Fort, and M. Modugno, Effective expression of the Lee-Huang-Yang energy functional for heteronuclear mixtures, Phys. Rev. A **100**, 063636 (2019).

[16] T. G. Skov, M. G. Skou, N. B. Jørgensen, and J. J. Arlt, Observation of a Lee-Huang-Yang Fluid, Phys. Rev. Lett. **126**, 230404 (2021).

[17] T. D. Lee, K. Huang, and C. N. Yang, Eigenvalues and eigenfunctions of a bose system of hard spheres and its low-temperature properties, Phys. Rev. **106**, 1135 (1957).

[18] L. M. Aycock, H. M. Hurst, D. K. Efimkin, D. Genkina, H.-I. Lu, V. M. Galitski, and I. B. Spielman, Brownian motion of solitons in a Bose–Einstein condensate, Proc. Natl. Acad. Sci. USA **114**, 2503 (2017).

[19] T. M. Bersano, V. Gokhroo, M. A. Khamehchi, J. DAmbroise, D. J. Frantzeskakis, P. Engels, and P. G. Kevrekidis, Three-Component Soliton States in Spinor $F = 1$ Bose-Einstein Condensates, Phys. Rev. Lett. **120**, 063202 (2018).

[20] A. R. Fritsch, M. Lu, G. H. Reid, A. M. Piñeiro, and I. B. Spielman, Creating solitons with controllable and near-zero velocity in Bose-Einstein condensates, Phys. Rev. A **101**, 053629 (2020).

[21] S. Mossman, G. C. Katsimiga, S. I. Mistakidis, A. Romero-Ros, T. M. Bersano, P. Schmelcher, P. G. Kevrekidis, and P. Engels, Observation of dense collisional soliton complexes in a two-component Bose-Einstein condensate, arXiv:2208.10585.

[22] X. Chai, D. Lao, K. Fujimoto, and C. Raman, Magnetic soliton: From two to three components with SO(3) symmetry, Phys. Rev. Res. **3**, L012003 (2021).

[23] K.-Xuan Yao, Z. Zhang, and C. Chin, Domain-wall dynamics in Bose–Einstein condensates with synthetic gauge fields, Nature (London) **611**, 68 (2022).

[24] L. Amico *et al.*, Roadmap on atomtronics: State of the art and perspective, AVS Quantum Sci. **3**, 039201 (2021).

[25] S. I. Mistakidis, A. G. Volosniev, R. E. Barfknecht, T. Fogarty, T. Busch, A. Foerster, P. Schmelcher, and N. T. Zinner, Cold atoms in low dimensions—a laboratory for quantum dynamics, arXiv:2202.11071.

[26] C. Chin, R. Grimm, P. Julienne, and E. Tiesinga, Feshbach resonances in ultracold gases, Rev. Mod. Phys. **82**, 1225 (2010).

[27] D. S. Petrov, Quantum Mechanical Stabilization of a Collapsing Bose-Bose Mixture, Phys. Rev. Lett. **115**, 155302 (2015).

[28] D. S. Petrov and G. E. Astrakharchik, Ultradilute Low-Dimensional Liquids, Phys. Rev. Lett. **117**, 100401 (2016).

[29] P. Zin, M. Pylak, T. Wasak, M. Gajda, and Z. Idziaszek, Quantum Bose-Bose droplets at a dimensional crossover, Phys. Rev. A **98**, 051603(R) (2018).

[30] T. Ilg, J. Kumlin, L. Santos, D. S. Petrov, and H. P. Büchler, Dimensional crossover for the beyond-mean-field correction in Bose gases, Phys. Rev. A **98**, 051604(R) (2018).

[31] M. R. Pathak and A. Nath, Dynamics of quantum droplets in an external harmonic confinement, Sci. Rep. **12**, 6904 (2022).

[32] A. Debnath, A. Khan, and S. Basu, Dropleton-soliton crossover mediated via trap modulation, Phys. Lett. A **439**, 128137 (2022).

[33] G. E. Astrakharchik and B. A. Malomed, Dynamics of one-dimensional quantum droplets, Phys. Rev. A **98**, 013631 (2018).

[34] T. Mithun, A. Maluckov, K. Kasamatsu, B. A. Malomed, and A. Khare, Modulational instability, inter-component asymmetry, and formation of quantum droplets in one-dimensional binary Bose gases, Symmetry **12**, 174 (2020).

[35] S. Saqlain, T. Mithun, R. Carretero-González, and P. G. Kevrekidis, Dragging a defect in a droplet Bose-Einstein condensate, Phys. Rev. A **107**, 033310 (2023).

[36] M. Tylutki, G. E. Astrakharchik, B. A. Malomed, and D. S. Petrov, Collective excitations of a one-dimensional quantum droplet, Phys. Rev. A **101**, 051601(R) (2020).

[37] E. Chiquillo, Low-dimensional self-bound quantum Rabi-coupled bosonic droplets, Phys. Rev. A **99**, 051601(R) (2019).

[38] A. Tononi, Y. Wang, and L. Salasnich, Quantum solitons in spin-orbit-coupled Bose-Bose mixtures, Phys. Rev. A **99**, 063618 (2019).

[39] N. Guebli and A. Boudjemâa, Quantum self-bound droplets in Bose-Bose mixtures: Effects of higher-order quantum and thermal fluctuations, Phys. Rev. A **104**, 023310 (2021).

[40] T. Mithun, S. I. Mistakidis, P. Schmelcher, and P. G. Kevrekidis, Statistical mechanics of one-dimensional quantum droplets, Phys. Rev. A **104**, 033316 (2021).

[41] P. Stürmer, M. N. Tengstrand, and S. M. Reimann, Mixed bubbles in a one-dimensional Bose-Bose mixture, Phys. Rev. Res. **4**, 043182 (2022).

[42] Z.-H. Luo, W. Pang, B. Liu, Y.-Y. Li, and B. A. Malomed, A new form of liquid matter: Quantum droplets, Font. Phys. **16**, 32201 (2021).

[43] A. Khan and A. Debnath, Quantum droplet in lower dimensions, Front. Phys. **10**, 887338 (2022).

[44] K. E. Wilson, N. Westerberg, M. Valiente, C. W. Duncan, E. M. Wright, P. Öhberg, and D. Faccio, Observation of Photon Droplets and Their Dynamics, Phys. Rev. Lett. **121**, 133903 (2018).

[45] J. G. M. Walker, G. R. M. Robb, G.-L. Oppo, and T. Ackemann, Dynamics of optomechanical droplets in a Bose-Einstein condensate, Phys. Rev. A **105**, 063305 (2022).

[46] M. Barranco, R. Guardiola, S. Hernández, R. Mayol, J. Navarro, and M. Pi, Helium nanodroplets: An overview, J. Low Temp. Phys. **142**, 1 (2006).

[47] A. Shukla, P. K. Neeraj, and P. K. Panigrahi, Kink-like solitons in quantum droplet, J. Phys. B: At., Mol. Opt. Phys. **54**, 165301 (2021).

[48] Y. V. Kartashov, V. M. Lashkin, M. Modugno, and L. Torner, Spinor-induced instability of kinks, holes and quantum droplets, New J. Phys. **24**, 073012 (2022).

[49] J. Kopyciński, M. Łebek, W. Górecki, and K. Pawłowski, Ultrawide Dark Solitons and Droplet-Soliton Coexistence in a Dipolar Bose Gas with Strong Contact Interactions, Phys. Rev. Lett. **130**, 043401 (2023).

[50] C. D'Errico, M. Zaccanti, M. Fattori, G. Roati, M. Inguscio, G. Modugno, and A. Simoni, Feshbach resonances in ultracold ^{39}K, New J. Phys. **9**, 223 (2007).

[51] E. Haller, M. Gustavsson, M. J. Mark, J. G. Danzl, R. Hart, G. Pupillo, and H.-C. Nägerl, Realization of an excited, strongly correlated quantum gas phase, Science **325**, 1224 (2009).

[52] L. Amico, D. Anderson, M. Boshier, J. P. Brantut, L. C. Kwek, A. Minguzzi, and W. von Klitzing, "*Colloquium*: Atomtronic circuits: From many-body physics to quantum technologies," Rev. Mod. Phys. **94**, 041001 (2022).

[53] G. Natale, T. Bland, S. Gschwendtner, L. Lafforgue, D. S. Grün, A. Patscheider, M. J. Mark, and F. Ferlaino, Bloch oscillations and matter-wave localization of a dipolar quantum gas in a one-dimensional lattice, Commun. Phys. **5**, 227 (2022).

[54] In the limit $\mu/\mu_{QD} \to 0$, Eq. (11), becomes $\mu/\mu_{QD} = (3N_{DQD}/N_0)^{2/3}$ and the root-mean-squared width, Eq. (10), is $\sqrt{\langle x^2 \rangle}/\xi_{QD} = \sqrt{(\pi^2 - 6)/9}(\sqrt{3}N_0/N_{DQD})^{1/3}$. This limit is appropriate for the quantum droplet [33].

[55] A. Richaud, V. Penna, R. Mayol, and M. Guilleumas, Vortices with massive cores in a binary mixture of Bose-Einstein condensates, Phys. Rev. A **101**, 013630 (2020).

[56] A. Richaud, V. Penna, and A. L. Fetter, Dynamics of massive point vortices in a binary mixture of Bose-Einstein condensates, Phys. Rev. A **103**, 023311 (2021).

[57] M. Edmonds, M. Eto, and M. Nitta, Synthetic superfluid chemistry with vortex-trapped quantum impurities, Phys. Rev. Res. **3**, 023085 (2021).

[58] R. Doran, A. W. Baggaley, and N. G. Parker, Vortex solutions in a binary immiscible Bose-Einstein condensate, arXiv:2207.12913.

[59] V. E. Zakharov and A. B. Shabat, Interaction between solitons in a stable medium, Zh. Eksp. Teor. Fiz. **64**, 1627 (1973) [Sov. Phys. JETP **37**, 823 (1973)].

[60] C. Becker, S. Stellmer, P. Soltan-Panahi, S. Dörscher, M. Baumert, E. Richter, J. Kronjäger, K. Bongs, and K. Sengstock, Oscillations and interactions of dark and dark–bright solitons in Bose–Einstein condensates, Nat. Phys. **4**, 496 (2008).

[61] A. Weller, J. P. Ronzheimer, C. Gross, J. Esteve, M. K. Oberthaler, D. J. Frantzeskakis, G. Theocharis, and P. G. Kevrekidis, Experimental Observation of Oscillating and Interacting Matter Wave Dark Solitons, Phys. Rev. Lett. **101**, 130401 (2008).

[62] G. Theocharis, A. Weller, J. P. Ronzheimer, C. Gross, M. K. Oberthaler, P. G. Kevrekidis, and D. J. Frantzeskakis, Multiple atomic dark solitons in cigar-shaped Bose-Einstein condensates, Phys. Rev. A **81**, 063604 (2010).

[63] D. K. Campbell, M. Peyrard, and P. Sodano, Kink-antikink interactions in the double sine-Gordon equation, Phys. D (Amsterdam, Neth.) **19**, 165 (1986).

[64] See Supplemental Material at http://link.aps.org/supplemental/10.1103/PhysRevResearch.5.023175 for animations corresponding to data presented in Figs. 6(c) and 6(e).

[65] M. I. Shaukat, E. V. Castro, and H. Terças, Quantum dark solitons as qubits in Bose-Einstein condensates, Phys. Rev. A **95**, 053618 (2017).

[66] N. Navon, R. P. Smith, and Z. Hadzibabic, Quantum gases in optical boxes, Nat. Phys. **17**, 1334 (2021).

[67] T. Busch and J. R. Anglin, Motion of Dark Solitons in Trapped Bose-Einstein Condensates, Phys. Rev. Lett. **84**, 2298 (2000).

[68] M. Ma, R. Navarro, and R. Carretero-González, Solitons riding on solitons and the quantum Newton's cradle, Phys. Rev. E **93**, 022202 (2016).

[69] T. Winiecki, J. F. McCann, and C. S. Adams, Vortex structures in dilute quantum fluids, Europhys. Lett. **48**, 475 (1999).

[70] T. Bland, M. J. Edmonds, N. P. Proukakis, A. M. Martin, D. H. J. O'Dell, and N. G. Parker, Controllable nonlocal interactions between dark solitons in dipolar condensates, Phys. Rev. A **92**, 063601 (2015).

[71] M. J. Edmonds, T. Bland, D. H. J. O'Dell, and N. G. Parker, Exploring the stability and dynamics of dipolar matter-wave dark solitons, Phys. Rev. A **93**, 063617 (2016)

[72] X. Chai, L. You, and C. Raman, Magnetic solitons in an immiscible two-component Bose-Einstein condensate, Phys. Rev. A **105**, 013313 (2022).

[73] https://github.com/quantummje/lhynewtonraphson.